

Experimental and Theoretical Explorations of Traveling Waves and Tuning in the Bushcricket Ear

Elizabeth S. Olson^{1,*} and Manuela Nowotny²

¹Columbia University, New York, New York and ²Goethe University, Frankfurt am Main, Germany

ABSTRACT The ability to detect airborne sound is essential for many animals. Examples from the inner ear of mammals and bushcrickets demonstrate that similar detection strategies evolved in taxonomically distant species. Both mammalian and bushcricket ears possess a narrow strip of sensory tissue that exhibits an anatomical gradient and traveling wave motion responses used for frequency discrimination. We measured pressure and motion in the bushcricket ear to investigate physical properties, stiffness, and mass, which govern the mechanical responses to sound. As in the mammalian cochlea, sound-induced fluid pressure and motion responses were tonotopically organized along the longitudinal axis of the crista acustica, the bushcricket's hearing organ. The fluid pressure at the crista and crista motion were used to calculate the acoustic impedance of the organ-bounded fluid mass (Z_{mass}). We used a theoretical wave analysis of wavelength data from a previous study to predict the crista acustica stiffness. The wave analysis also predicts Z_{mass} , and that result agreed reasonably well with the directly measured Z_{mass} , lending support to the theoretical wave analysis. The magnitude of the crista stiffness was similar to basilar membrane stiffness in mammals, and as in mammals, the stiffness decreased from the high-frequency to the low-frequency region. At a given location, the stiffness increased with increasing frequency, corresponding to increasing curvature of the traveling wave (decreasing wavelength), indicating that longitudinal coupling plays a substantial role in determining crista stiffness. This is in contrast to the mammalian ear, in which stiffness is independent of frequency and longitudinal coupling is relatively small.

INTRODUCTION

Like the cochlear hearing organs of mammals, the hearing organ of katydids (bushcrickets), called the crista acustica, features a smooth gradient of anatomical properties along its length (1–9). Upon sound stimulation, the crista acustica responds with mechanical traveling waves (10–13), and as in the mammalian cochlea, the traveling waves peak at different longitudinal locations, producing a tonotopic map (2,14–21). Along the 1-mm length of sensory tissue in the crista acustica of *Mecopoda elongata*, frequencies ranging from 3 to 80 kHz are processed, with the lower frequencies represented in the proximal region and the higher frequencies in the distal region. The longitudinal variation in anatomical parameters in *M. elongata* predicts this trend, with the anatomy of the distal, high-frequency region consistent with greater stiffness and the anatomy of the proximal, lower-frequency region consistent with greater compliance (9).

Previously, findings (Fig. 3 of Palghat Udayashankar et al. (10)) demonstrated a tonotopically tuned traveling wave

along the bushcricket crista acustica. These data are redrawn in Fig. 1. The x axis is longitudinal location, distal (high-frequency region) to the left and proximal (low-frequency region) to the right. The top row shows the amplitude and the bottom row the phase, with each column a different stimulus frequency, ranging from 6 kHz (*far right panel*) to 60 kHz (*far left panel*). Several spurious data points were removed without changing the shape of the curves that is emphasized in this analysis. The 6 kHz result peaks at the very proximal edge of measurement. Other frequencies, from 9 to 60 kHz, show clear amplitude maxima, with each higher frequency peaking further distal. Proximal to each peak, there is a plateau in the amplitude and phase response. Distal to the plateau, the phase goes through a fairly smooth progression through approximately a complete cycle (~ 6 radians), characteristic of a traveling wave. The value of the phase decreases quite smoothly from the distal to the proximal region, indicating the direction of wave travel is from the distal, high-frequency region to the proximal, low-frequency region—from left to right in Fig. 1.

To illustrate the wave and plateau, Fig. 2 shows the 21 kHz data plotted as amplitude $\times \sin(\text{phase} + \text{shift}(n))$ at five times in the cycle, by letting $\text{shift}(n) = n \times 2\pi/6$ with n taking integer values from 1 to 5. The wave is clear, and the plateau

Submitted July 19, 2018, and accepted for publication November 21, 2018.

*Correspondence: eao2004@columbia.edu

Editor: James Keener.

<https://doi.org/10.1016/j.bpj.2018.11.3124>

© 2018 Biophysical Society.



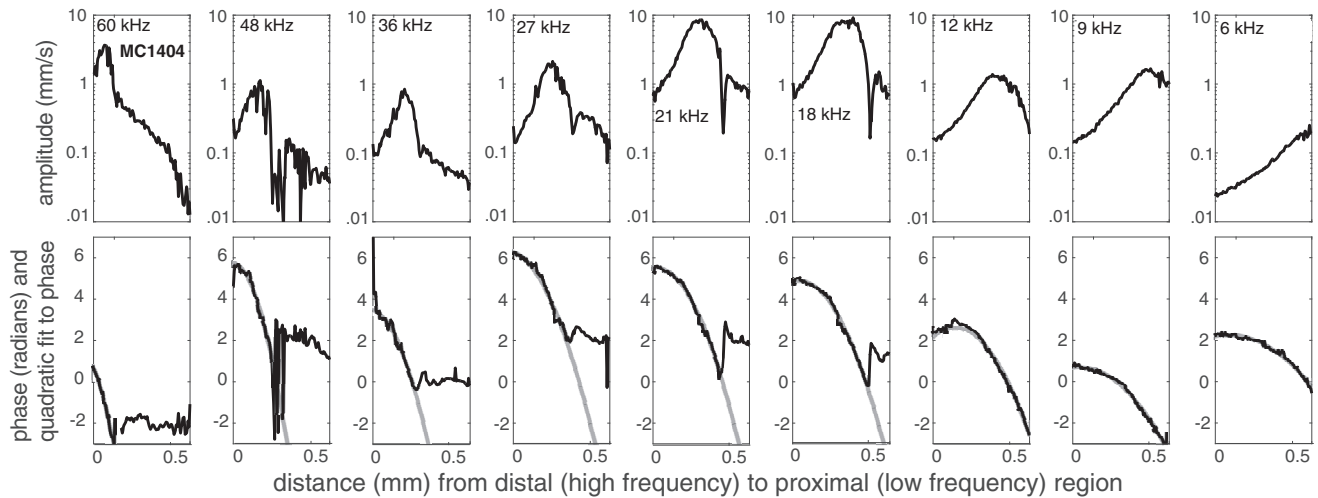


FIGURE 1 Velocity amplitude (*top row*) and phase (*bottom row*) versus distance along the organ, animal MC1404. Stimulus level was 80 dB SPL at the spiracle (EC) opening. Each column shows data from a different stimulus frequency, noted in the legend. Experimental data are in black, and in gray in the bottom row are quadratic fits to the phase data. Only data in which the phase excursion indicates the presence of a traveling wave were used in the fit; data in the plateau region were excluded. Data are from Palghat Udayashankar et al. (10).

region on the right has a much smaller amplitude than at the peak of the wave but still moves in a uniphasic, piston-like fashion. The plateau motion in the proximal region is nearly exactly out of phase (π radians) with the distal motion on the far left. This uniphasic plateau motion could be a standing wave that appears because of reflection of the traveling wave or it could be a direct (nontraveling) response to the driving pressure. There is also a plateau in motion in mammals at regions beyond the traveling wave peak (22).

In the mammalian cochlea, computational and physical models have shown that the formation of traveling waves

is based on fluid mass and tissue stiffness (23,24). The fluid mass provides inertia and longitudinal coupling, and the stiffness of the organ of Corti complex (which includes the cellular organ of Corti and the basilar and tectorial membranes) provides a restoring force. Anatomical gradients are present and provide the longitudinally varying stiffness that is key to tonotopic tuning (23,25–28).

As in the mammalian organ of Corti, the sensory cells in the bushcricket crista acustica are embedded in a complex structure of supporting cells (Fig. 3). One single unit with one bipolar sensory neuron is called a scolopidium. A scolopale cell that surrounds the ciliated dendrite of the bipolar neuron with scolopale rods also belongs to this unit. A cap cell sitting on top of the dendrite anchors the tip of the dendrite in a rigid cap. These scolopidia are arranged in a single row that is covered by an acellular membrane, called the tectorial membrane. Anatomical investigations showed side bands in this cover membrane (Fig. 3 D) (29), and it is supposed that the tectorial membrane is responsible for longitudinally coupling the sensory units of the crista acustica (2). The lower surface of the crista acustica is supported by the dorsal wall of the acoustic trachea, an acellular cuticular structure (30). The dorsal wall had been forwarded as the dominant stiffness that the stimulating sound pressure works against (similar to the mammalian basilar membrane) (4), but this was disputed by anatomical measurements that indicated that cellular structures are likely to govern the longitudinal stiffness gradient (9). Results of this study estimate the value of the stiffness but do not speak to the dominant source of the stiffness.

In the bushcricket crista acustica, the biophysical basis for the slow traveling wave is likely similar to that in the mammalian cochlea (fluid mass and tissue stiffness), but

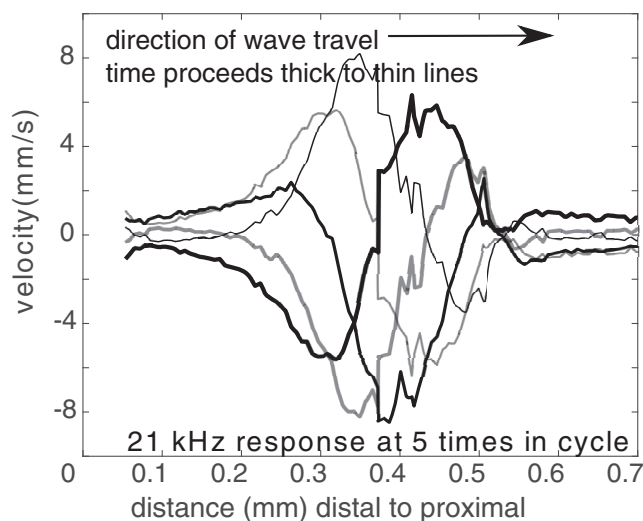


FIGURE 2 The 21 kHz response from Fig. 1 at five times in the cycle, spaced by $\pi/3$ radians (one sixth of a cycle). The wave proceeds from the distal to the proximal locations, left to right in the figure (*thicker to thinner curves alternating black and gray*). Data are from Palghat Udayashankar et al. (10).

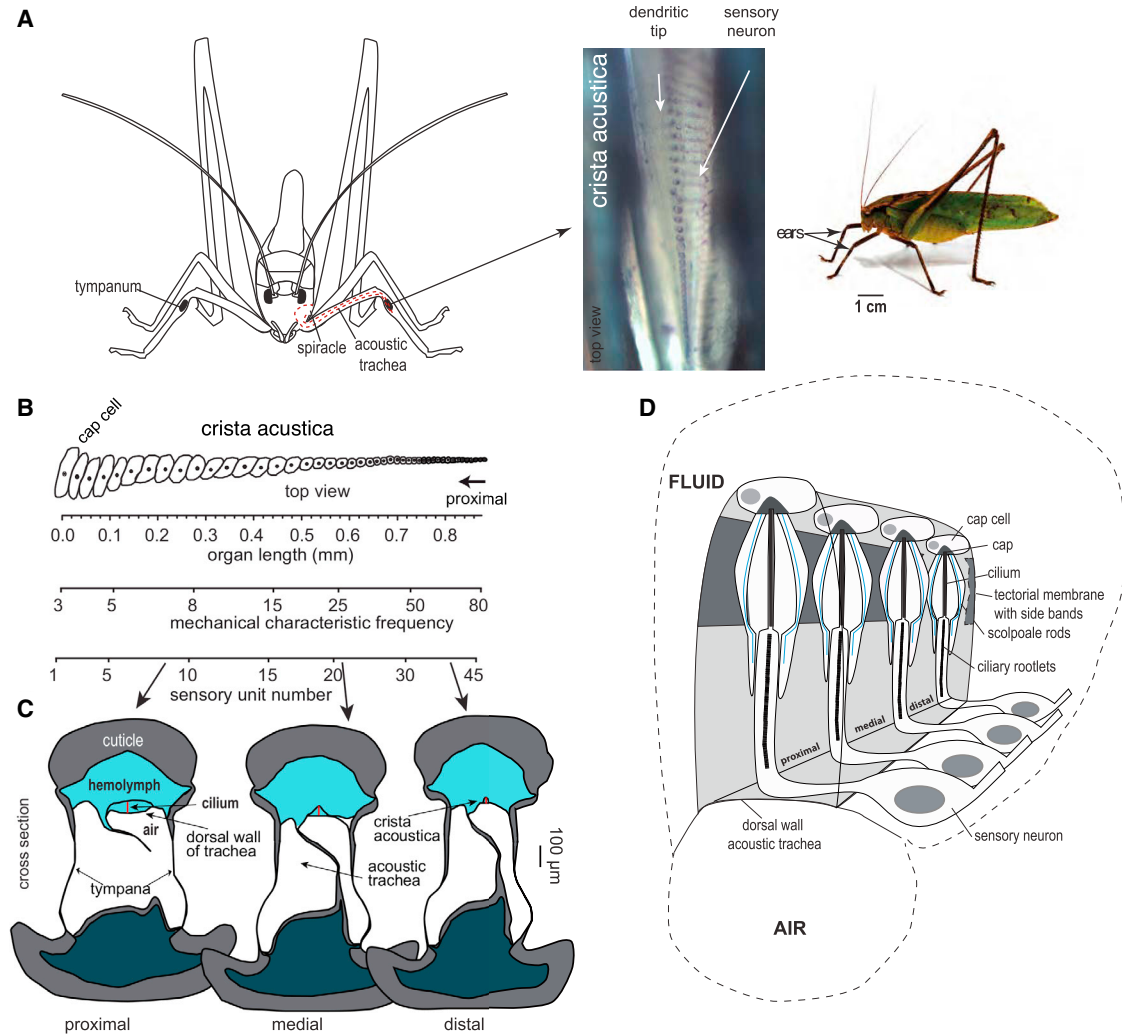


FIGURE 3 The bushcricket ear. (A) An acoustic trachea is open to air on one end, the spiracle, which is like the EC opening in the mammal. There are also two tympana (anterior and posterior) in each foreleg (see (C)). (B) Behind the tympana, but not attached to them, there is a linearly arranged hearing organ, called the crista acustica, which contains ~ 45 sensory units in the species *M. elongata*. (C) Cross sections through the ear at three longitudinal locations show the longitudinally varying anatomy. (D) A schematic drawing of the crista acustica. To see this figure in color, go online.

some aspects, particularly those related to longitudinal coupling, might be different. We sought to understand the physical properties that underlie traveling waves and tonotopic tuning in the bushcricket ear. To that purpose, we measured the sound-induced motion of, and fluid pressure above, the crista acustica. We coupled the measurements and previous measurements of motion to traveling wave theory and determined the size and character of the stiffness of the crista acustica and its support structure.

METHODS

We performed experiments with eight adult male and female bushcrickets of the tropical Southeast Asian bushcricket species *M. elongata* L. (Insecta, Orthoptera, Tettigoniidae). The animals were bred in a colony at the Department of Cell Biology and Neuroscience in Frankfurt am Main (Germany) and transported to the Fowler Memorial Laboratory at Columbia University

(New York, NY). This was authorized by the U.S. Department of Agriculture. Several of the animals were used in preliminary measurements. We show and analyze data from the two most complete data sets, and the analysis also uses previously published data (10).

The animals were anesthetized with CO_2 , and wings, mid, and hind legs were removed. Body and forelegs were fixed by rosin wax in a ringer-filled bath chamber, and then the leg cuticle above the crista acustica was removed to expose the crista. This procedure leaves the crista acustica intact, including the tectorial membrane. Based on both theoretical reasoning and control measurements, the effect of this opening is not expected to cause a great disturbance in the pattern of organ motion. Firstly, in traveling wave theory, when the wavelength/ (2π) is less than the fluid height, the wave can be considered in a “short wave” regime in which the fluid height is not critical (23). In the bushcricket ear, the traveling wave wavelength is ~ 0.4 mm (Figs. 1 and 2). With this, as long as the fluid height is greater than ~ 0.07 mm, the condition is satisfied (Fig. 3 C). Secondly, in control measurements in which distortion product otoacoustic emissions responses were measured before and after removal of the cuticle, changes in responses varied, but the variations could be small (10). With these considerations, the necessary removal of the cuticle was deemed reasonable.

Pressure was measured with a fiber optic pressure sensor, with outer diameter 125 μm and sensing area diameter 75 μm . It is shown to scale in Fig. 4 A. The sensors are calibrated in a fluid shaker before each experiment, and their responses are reasonably flat with frequency through 50 kHz (31,32). The width of the sensing area is slightly smaller than 0.25 wavelength of the traveling wave. The sound-induced vertical motion of the crista acustica was measured in two ways, illustrated in Fig. 4: 1) using spatial pressure differences to estimate the fluid acceleration at the surface of the crista acustica, which is then further analyzed to find velocity or displacement, and 2) with a velocity-sensitive Laser-Doppler-Vibrometer (LDV) (OFV-534 and OFV-5000 VD06; Polytec, Waldbronn, Germany). The LDV has a flat frequency response. Although method 2 is more accurate, method 1 has the benefit of being able to provide simultaneous measurements of pressure and motion to calculate their ratio, which is the specific acoustic impedance of the organ-bounded overlying fluid. To briefly explain method 1 (further explanation is in (31)), the fluid is saline-like. Saline has low enough viscosity that at frequencies above several kHz, fluid motion is governed by the inviscid, linear Navier-Stokes equation, which in one dimension (vertical direction in Fig. 4) is $dP/dx = -\rho a_x$. a_x is the fluid acceleration in the x direction, and ρ is the fluid density, taken to be that of water ($\sim 1000 \text{ kg/m}^3$). With pure-tone stimulus and response of frequency f (radian frequency, $\omega = 2\pi f$), velocity ($v_x = a_x/i\omega$). The tissue must move with the adjacent fluid, so the fluid velocity close to the sensory tissue is approximately equal to the crista acustica velocity. The spatial difference was made with the closer location $\sim 10\text{--}20 \mu\text{m}$ from the sensory tissue and the further location 20 μm further back. The viscous boundary layer thickness is $\sim 3 \mu\text{m}$ at 10 kHz and varies as $1/\sqrt{f}$, and because the calculation described above assumes viscous forces are dominated by inertial forces, the closest measurement should be made outside this layer. Thus, pressure, P , and velocity, v_x , can be found simulta-

neously at the same location. Together, these were used to measure the specific acoustic impedance of the fluid, $Z_{fluid} = P/v_x$, at the sensory tissue. As described further below, in theory, Z_{fluid} depends on the fluid density and viscosity, the dimensions of the organ that bound the fluid, and the wavelength of the traveling wave. Z_{fluid} will have real and imaginary parts, with the imaginary part corresponding to the mass of fluid that moves with the tissue, the “effective fluid mass” (24).

Pressure and velocity measurements were made at several positions along the tonotopic longitudinal axis of the hearing organ: proximal, medial, and distal. The velocity measurements with the LDV at approximately the same positions provided a control velocity measurement and were performed before and after the pressure measurements. The same acoustic stimulation parameters were used for the pressure and LDV measurements. Pure-tone stimuli (1–50 kHz, each tone 1 s duration) were broadcast by a loudspeaker (Fostex Super Tweeter; Fostex, Tokyo, Japan) in an open field situation, $\sim 30 \text{ cm}$ away from the bushcricket spiracle (Fig. 3 A). The spiracle is the ear canal (EC) opening to the trachea and is abbreviated EC in figure labels. An ultrasonic Sokolich probe tube microphone (WGS and Associates, Newport Beach, CA) with a flat frequency response, positioned at the spiracle, was used for setting the stimulus level at the spiracle accurately and measuring it during the experiment. Stimulation levels were at 60- and 80-dB sound pressure level (SPL). A Tucker Davis Technologies RX6 (Tucker-Davis Technologies, Alachua, FL)—operating at a sampling rate of 200 kHz, coupled to a PA5 attenuator and HB7 headphone buffer—was used for stimulus generation and data acquisition. Data were referenced to the sound stimulus measured at the spiracle.

One of the fundamental quantities of wave mechanics is the wavenumber, k , also termed “curvature” because it represents the curviness of the wave. By definition, the derivative of the phase with longitudinal location, $d\phi/dx$, is the local wavenumber, k . In the simple case in which k is constant with

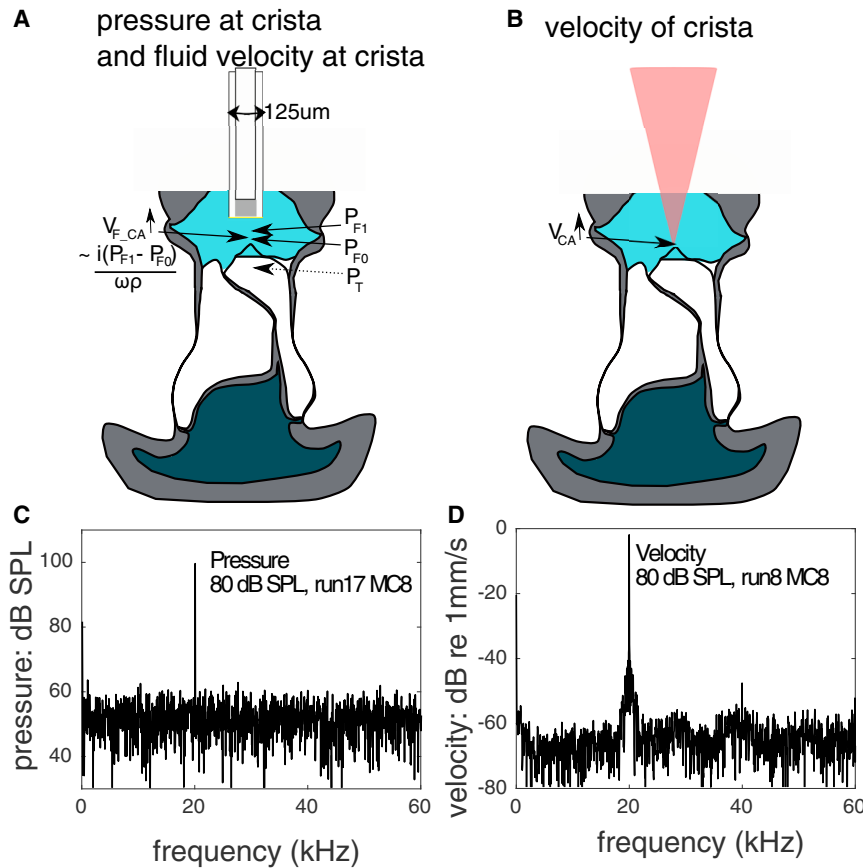


FIGURE 4 (A) With a pressure sensor above the crista acustica, the fluid pressure was measured at different distances to the hearing organ (P_{F0} , P_{F1} , ...). Pressure differences were used to estimate the fluid velocity at the crista surface ($V_{F,CA}$). (B) The velocity of the sound-induced organ motion was measured with an LDV before and after fluid pressure measurements to check repeatability. (C) Pressure data set, with an 80 dB SPL, 20 kHz stimulus. Response was $\sim 100 \text{ dB SPL}$. Noise level is $\sim 60 \text{ dB SPL}$. (D) Velocity data set, with an 80 dB SPL, 20 kHz stimulus. Response was close to 1 mm/s. Noise level was $\sim 0.001 \text{ mm/s}$. To see this figure in color, go online.

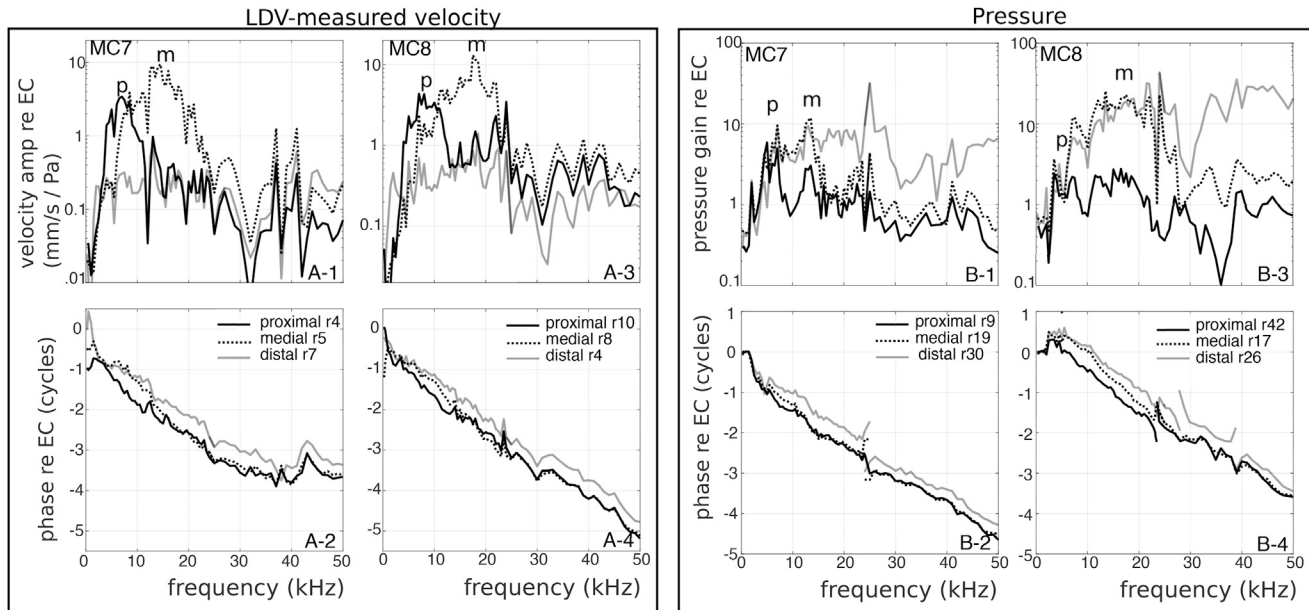


FIGURE 5 Sound-induced organ velocity and fluid pressure at the crista acustica. Data from two animals are shown. (A) Using the LDV, the crista acustica velocity was measured in the proximal, medial, and distal regions. The upper graphs (A-1 and A-3) show the sound-induced amplitude of the organ velocity, and the lower graphs (A-2 and A-4) show the corresponding phase response. Both amplitude and phase are shown relative to the stimulus measured at the spiracle (termed EC for ear canal). (B) In the same animals, sound-induced fluid pressure above the crista acustica was measured by the fiber-optic pressure sensor. The upper graphs (B-1 and B-3) show the amplitude gain of the fluid pressure and the lower graphs (B-2 and B-4) the pressure phase relative to the stimulus. The “m” and “p” notations in the upper graphs indicate the amplitude maximum in the medial and proximal regions. A clear maximum was not apparent in the distal measurements, and thus we do not include a “d.”

location, this derivative is simply a division, resulting in the familiar result, $k = 2\pi/\lambda$. For the data in Fig. 1, quadratic fits to the data were found (*light gray curves*), so $\varphi(x) = \varphi_0 + ax + bx^2$. Higher-order polynomial fits were not needed. From the quadratic fits, $k(x) = a + 2bx$.

RESULTS

Crista acustica velocity and fluid pressure measurements

Results from all preparations in which pressure and velocity were measured were similar on key points, and results from two preparations are shown. The LDV-based measurements of the sound-induced organ velocity (Fig. 5 A) confirmed previous findings that showed a tonotopic shift in amplitude maxima from lower frequencies in the proximal to higher frequencies in the medial and then distal parts of the organ. The velocity in the proximal region peaked at ~ 8 kHz and in the medial region at ~ 15 – 17 kHz in both preparations; these peaks are marked by m (medial) and p (proximal) symbols. The velocity in the distal region lacked a distinct amplitude peak and was generally smaller in magnitude than in the proximal and medial regions. The distal region best frequency might have been more than the 50 kHz maximum of the current measurements. Fluid pressure measurements (Fig. 5 B) showed peaks in the medial and proximal regions at approximately the same frequencies as the LDV-measured velocities (m and p notations). The pressure peaks were less pronounced than the velocity peaks, particularly in

the proximal region. The distal region showed a relatively flat frequency response in the pressure, similar to the distal region responses in the velocity. However, the pressure magnitude was larger in the distal than the medial or proximal regions, which is different from the observation in velocity. This was particularly evident at frequencies >30 kHz, which is above the frequency at which the motion peaks in the medial and proximal regions.

Both pressure and velocity showed phase delay relative to the stimulus pressure measured at the spiracle (EC opening), and the approximately straight phase-frequency curve indicates an approximately constant delay of ~ 70 μ s. This is mainly acoustic delay through the ~ 2 -cm long acoustic trachea of the bushcricket (Fig. 3 A). Superimposed on this acoustic delay, at frequencies below ~ 18 kHz, by looking at a single frequency, one observes the phase delay increasing by >0.5 cycle from proximal to medial to distal locations. This is the traveling wave delay that is clearly observed in the longitudinal scans of Fig. 1. In Fig. 6, we redraw a subset of the velocity data from this experiments to compare with a subset of the previous data in Fig. 1. We show results with a stimulus frequency of ~ 12 kHz. This is a relatively low frequency in the bushcricket, and the traveling wave occupies most of the crista’s length before transitioning to a non-traveling-wave plateau, so the phase varies systematically from distal to medial to proximal locations. Responses at a stimulus frequency of 10.5 kHz are shown for MC7 and at a stimulus frequency of 12 kHz for

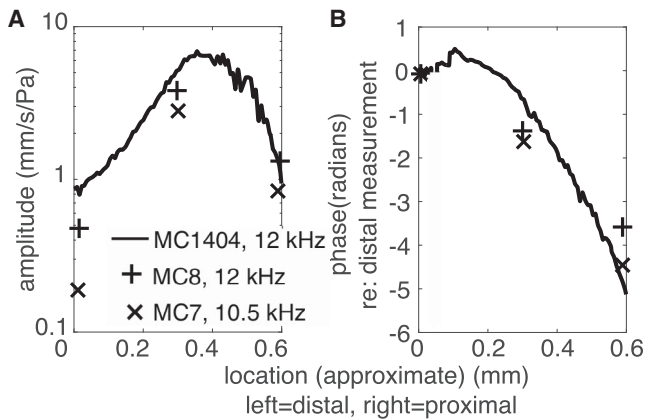


FIGURE 6 Subset of velocity data from Fig. 5, replotted at one frequency and the three measurement locations (distal, medial, proximal) and with 12 kHz data from Fig. 1 to directly compare the results from the two projects. (A) Amplitude. (B) Phase relative to distal location. The data from Fig. 5 are the + and × symbols; the data from Fig. 1 are the solid line. Fig. 1 data from Palghat Udayashankar et al. (10).

MC8 (+ and × symbols). There were three longitudinal locations in the MC7 and MC8 data sets, and the x axis locations for these data are approximate. The 12 kHz results from Palghat Udayashankar et al. (11) MC1404 (Fig. 1) are shown in the solid line, with the amplitude normalized to the 80-dB stimulus level. Fig. 6 demonstrates consistency between the data sets from the previous experimental studies and this experimental study.

At frequencies through the peak region, fluid pressure decreased as the distance from the surface of the crista acustica increased, as shown in a medial region measurement in Fig. 7. This is as expected because the pressure is expected to decrease with distance from the tissue surface of the traveling wave (23,33). At frequencies well above the peak (>30 kHz), there was a pressure plateau at which this expected behavior was no longer observed. Referring to Fig. 1, at frequencies >30 kHz, the medial region is no longer moving with the traveling wave that we are primarily interested in. We speculate that a pressure standing wave is involved in this observation or a transition from a traveling wave to a standing wave.

Finding the specific acoustic impedance of the fluid

In Fig. 8, we compare the crista acustica velocity measured with the LDV to the velocity measured using the pressure difference method described in Methods to illustrate the reasonable accuracy of the pressure difference method for measuring velocity. Fig. 8, A and B show the two pressure measurements that went into the velocity calculation, and Fig. 8, C and D show the calculated velocity in the solid line and the direct LDV-measured velocity in the dotted line. The agreement is reasonable in amplitude and phase in the region of the traveling wave peak (~ 5 – 27 kHz),

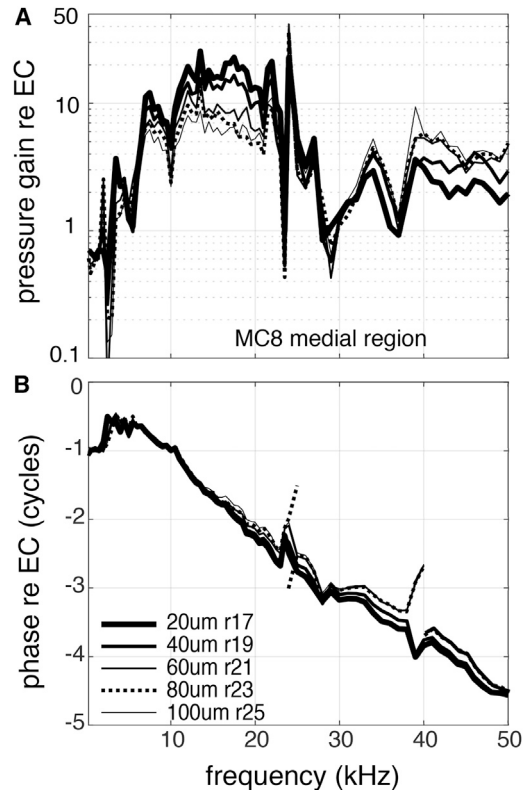


FIGURE 7 The fluid pressure measured at various distances from the surface of the crista acustica sensory tissue as the sensor was moved upward at a medial position. (A) Amplitude gain re EC. (B) Phase re EC.

giving credence to the pressure-difference method for measuring tissue motion. (At frequencies below 5 kHz, the pressure values are very similar at the two locations, and the pressure difference this velocity measurement relies on is therefore not reliable. This is apparent in that the black and gray lines are essentially overly below ~ 5 kHz in Fig. 8 A. To quantify this, from the data in Fig. 8 A, at frequencies below 5 kHz, the average pressure difference is only 0.6 dB, with an SD of 2.5 dB).

To accurately measure the specific acoustic impedance of the organ-bounded fluid, Z_{fluid} , temporally and spatially coincident pressure and velocity measurements are required, and this was possible when using the pressure measurements for both pressure and velocity. Z_{fluid} results from animals MC7 and MC8 at the distal and medial regions are shown in Fig. 9. Fig. 9, A and B show the distal region for the two animals, and Fig. 9, C and D show the medial region. Z_{fluid} is plotted as real and imaginary parts. The imaginary part was positive, as expected, because the impedance due to mass is imaginary and positive. Thus, the imaginary part of Z_{fluid} represents the mass of the fluid, and we refer to this part as organ-bounded fluid mass (Z_{mass}). As will be discussed further below, theoretically $Z_{mass} = i\omega m_{eff} = i\omega\rho \times h_{eff}$, where ρ is the fluid density and h_{eff} has a value that depends on wavelength and the dimensions of the fluid

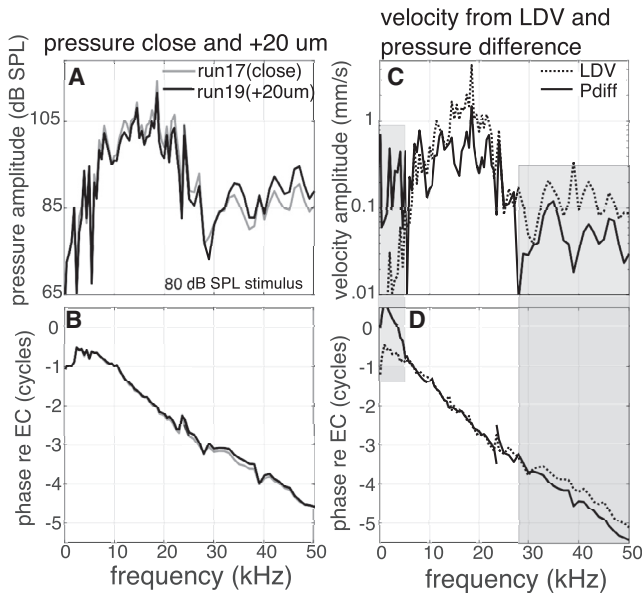


FIGURE 8 Velocity of the crista acustica found with the LDV and with pressure differences, MC8. Left shows pressure measurements close to ($\sim 10\text{--}20\ \mu\text{m}$) and $20\ \mu\text{m}$ further back from the crista acustica, amplitude in (A) and phase in (B). Right shows comparison of the velocity found with pressure difference calculation and with LDV in the same preparation, amplitude in (C) and phase in (D). Gray regions are less reliable because of very small pressure differences (low frequencies) and anomalous pressure variations (high-frequency plateau region noted in text).

channel (23,24). In the results of Fig. 9, Z_{mass} has a value of $\sim 5\ \text{Pa}/(\text{mm}/\text{s})$, without a robust frequency dependence. The value of Z_{mass} is slightly larger in the distal than in the medial region. This, to our knowledge, novel measurement of the size of Z_{mass} is the primary analytical result from the pressure and velocity measurements. This measurement was an objective of the study, which explores the traveling wave's basis in tissue stiffness and fluid mass. Another observation from Fig. 9 is that the real term, which represents resistance, tends to be negative. Passive resistance is positive, and we expected the real part of Z_{fluid} to be positive. The unexpected observation of negative resistance, if it is erroneous, could have been produced by an error in the relative pressure-velocity phase of ~ 0.25 cycle, a fraction of the 5+ cycle excursions in the data. We mitigated this potential error by making simultaneous pressure and voltage measurements, but it remains to some extent. The magnitude of the Z_{fluid} measurement is not sensitive to small phase errors and thus is more reliable, and we will find this quantity in a completely different way in the wave analysis to follow. The blue transparent lines anticipate the findings from the wave analysis.

Theoretical wave analysis provides an independent measure of fluid impedance

In the section above, we used measurements of pressure and velocity to find Z_{mass} . In the sections below, we use concepts

from wave mechanics and the data from Fig. 1 (from Palghat Udayashankar et al. (10)) to predict the Z_{mass} that was measured relatively directly in these experiments (Fig. 9). We compare the Z_{mass} values found in the two ways and finally use the wave analysis to characterize the stiffness of the crista acustica.

$k(x)$, found from the quadratic fits to the phase in Fig. 1 as described in the last paragraph of the Methods, is shown for the data in Fig. 1 in Fig. 10. The different colors are the different frequencies (*color online only*). (Note: $k(x)$ is only shown for points in the traveling wave region of the particular frequency; the plateau region points were excluded. In addition, for the relatively low frequencies, 6, 9, and 12 kHz, the fits were not very good in the distal region. For example, by referring to Fig. 1, we see that the 12 kHz parabolic fit has a maximum and reverses slope in the distal region where the phase data is nearly flat. Thus, the 6, 9, and 12 kHz k results have been restricted to the more proximal region. In the same vein, the 18 and 21 kHz k fits are not very good in the very distal region. We did not eliminate these distal points and simply note that the 18 and 21 kHz k values are not very reliable in the distal region.) The increasing k from distal to proximal locations is due to the fact that as the wave travels along (distal to proximal), its wavelength shortens. Also, at any one location, k increases with frequency, except for a few points in the very distal region.

Further theoretical analysis leading to the stiffness of the crista acustica

A mechanical wave is based on a balance of potential energy (PE) and kinetic energy (KE), simply written as $PE = 1/2Sx^2$ (S is stiffness, x is displacement) and $KE = 1/2mv^2 = 1/2mx^2\omega^2$ ($m = \text{mass}$, $v = \text{velocity}$). Equating PE and KE allows one to make predictions about wave properties (34). To introduce this section with a textbook example, in a string wave, the mass of interest is the string's mass density (mass per length), and for fixed displacement amplitude and varying frequency, because mass density does not change, KE grows as ω^2 . As anyone who has rhythmically shaken an extended string or slinky knows, as drive frequency increases, λ decreases. Thus, curvature, k , increases. Because of the longitudinal tension in the string, increased curvature increases stiffness: stiffness (S) is proportional to k^2 in a string wave. Taking $KE = PE$ leads to the result that k increases linearly with ω , and $d\omega/dk$ is constant, independent of frequency; wave speed is independent of frequency in a string wave. The fluid and tissue wave of the cochlea is also based on the underlying principle of $KE = PE$. In the mammalian cochlea, the structural elements of the basilar membrane are not longitudinally coupled, and the basilar membrane stiffness is not λ dependent. (Some cochlear models (35) do include a degree of cell-based longitudinal coupling, but this is not

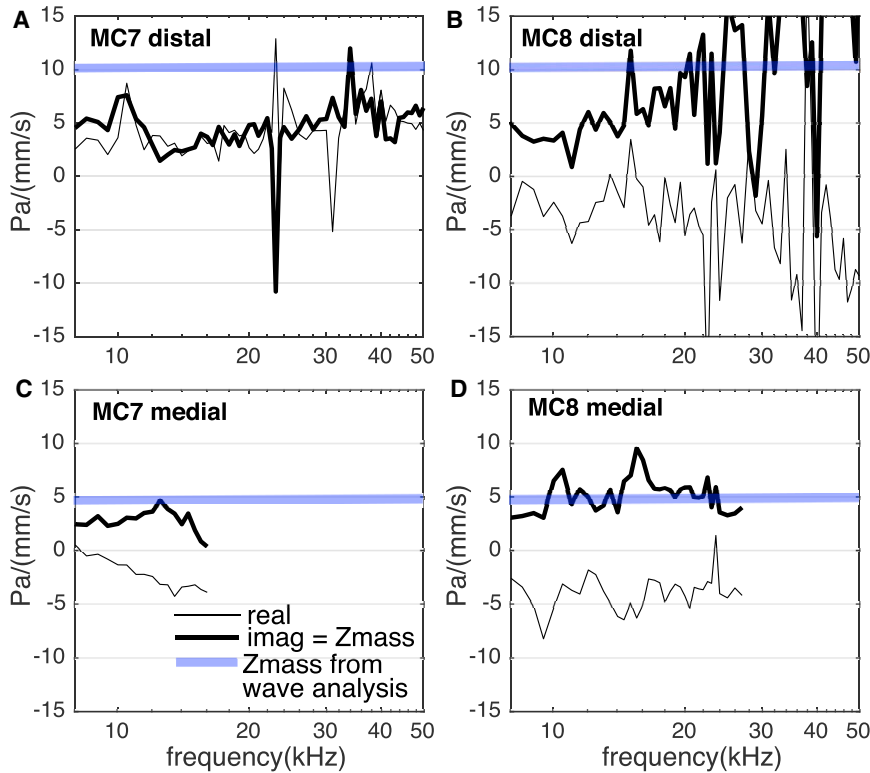


FIGURE 9 Specific acoustic impedance of the fluid, found as $Z_{fluid} = \text{pressure at the crista acustica surface} / \text{velocity of fluid at the crista acustica surface}$. Left panels are from animal MC7, right from MC8. Distal region is in (A) and (B), medial region (C) and (D). Z_{fluid} is plotted as real and imaginary parts. The imaginary part of Z_{fluid} represents the impedance of the fluid mass, Z_{mass} . The horizontal blue lines anticipate the value of Z_{mass} that emerges from the wave analysis. To see this figure in color, go online.

the dominant stiffness). For PE and KE to remain equal as frequency increases, the mass decreases with frequency. This happens because the mass in the cochlear wave system is predominantly fluid mass, and the effective fluid mass (m_{eff}) is smaller for shorter wavelengths (larger k).

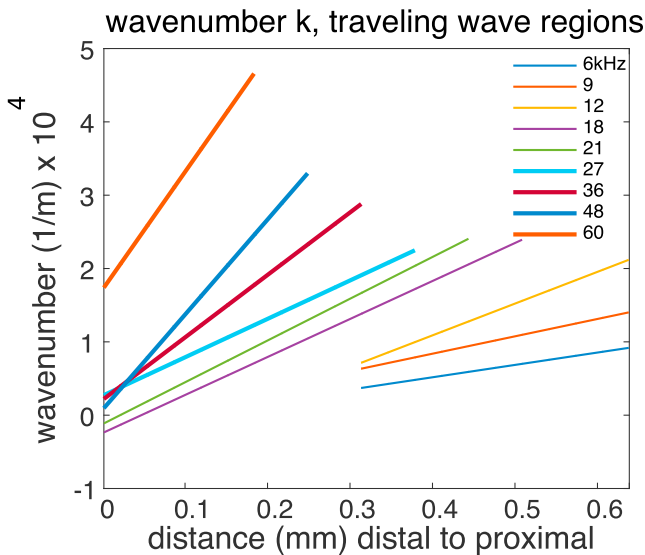


FIGURE 10 Wavenumber (k) as a function of distance, found with phase results from Fig. 1. Different frequencies are coded by color. At each frequency, k values are only shown for the traveling wave region where wavenumber is a useful concept. To see this figure in color, go online.

To explore the physical basis for the traveling wave in the bushcricket ear, we use the k values we have found to predict the form of m_{eff} . As noted when discussing Fig. 9, $m_{eff} = \rho h_{eff}$, where h_{eff} , the effective fluid height, is a function of wavenumber, k . h_{eff} also depends on the width and height of the fluid chamber and the width of the moving tissue surface (23,24). For a two-dimensional (2D) “deep-water wave” (for which the depth is greater than $\sim \lambda/(2\pi)$ and there are no lateral boundaries), the effective height is very simple: $h_{eff-2d-deep} = 1/k$ (23,36). A wave in a finite duct like the cochlea or crista acustica generally requires a three-dimensional (3D) treatment. After work from the mammalian cochlea, we took the duct height and width equal to each other to reduce the number of parameters and used $250 \mu\text{m}$ for this dimension, h . The fraction of the width of the duct taken up by compliant tissue (the sensory tissue), ϵ , was taken as 0.3. With the 3D treatment, h_{eff} is found as a series solution. We used a polynomial approximation to the series solution that (37) proposed:

$$h_{eff} = (\epsilon / (hk^2)) (1 + b(kh)^2) / (1 + \epsilon bkh).$$

The polynomial solution contains a parameter, b , chosen so that the series solution and approximate solution agree. b was taken as 1.2, and the agreement was checked by comparing the series and approximate solutions with 10 entries in the series solution. We used these b , ϵ , and h parameter values and k from Fig. 10 to calculate $h_{eff}(k)$, with the result in Fig. 11 A. The results from the 2D and 3D models

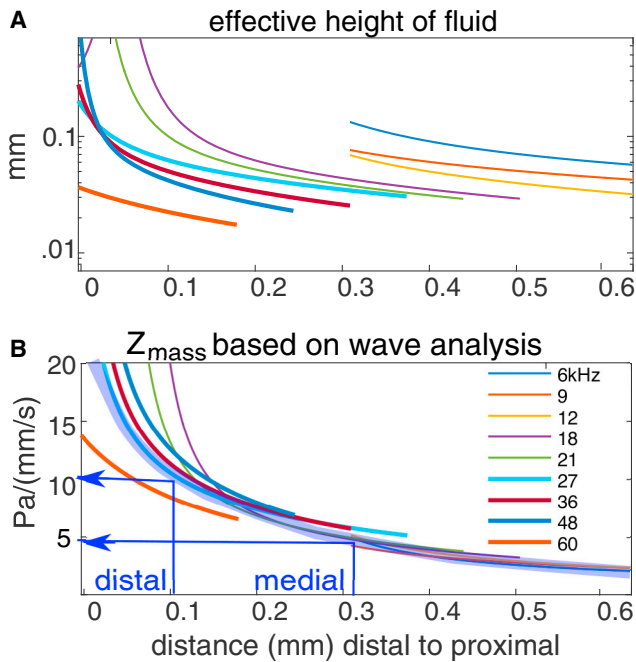


FIGURE 11 Effective height and fluid impedance, calculated from k data. (A) The “effective fluid height,” h_{eff} , of the wave. (B) Effective impedance because of the mass of the fluid, Z_{mass} . The thick blue line indicates the frequency-independent trend. Thin blue perpendicular lines with horizontal arrows identify Z_{mass} values at distal and medial locations. These values were included as blue horizontal lines in Fig. 9. To see this figure in color, go online.

were qualitatively similar (2D not shown), with quantitative differences of a factor of ~ 2 or less. Thus, the values of ε , h , and b are not very influential to the basic findings. Some observations can be made: at a given location, h_{eff} is larger for the lower frequencies. This is due to the decreasing k with decreasing frequency. At a given frequency, h_{eff} decreases from the distal location to the proximal location. This is due to the decreasing $\lambda = \text{increasing } k$ as the wave travels from the distal to the proximal region.

From h_{eff} , we can predict the mass component of the impedance of the fluid, Z_{mass} . The impedance due to fluid mass is $Z_{\text{mass}} = i\omega m_{\text{eff}} = i\omega\rho h_{\text{eff}}$, where the imaginary i indicates a phase of $\pi/2$. Thus, $|Z_{\text{mass}}|$ (units Pa/(m/s)) = $\rho h_{\text{eff}}\omega$. Z_{mass} is expected to be the dominant component of the fluid impedance, Z_{fluid} , because resistive components due to fluid viscosity are not expected to be dominant or the wave would be very damped. In Fig. 11 B, Z_{mass} is plotted. Z_{mass} varies from ~ 2 Pa/(mm/s) at the most proximal (low frequency) location to ~ 20 Pa/(mm/s) at the most distal (high frequency) location. Not all frequencies are available at all locations, but the curves all weave together to form a nearly frequency-independent line. At the most distal region, the lines are less tight, but the variability is partly due to the 18 and 21 kHz data, which, as noted above, were less reliable in the very distal region. The overlying transparent blue line indicates the frequency-independent trend, and the perpendicular

thin blue lines identify the Z_{mass} values at distal and medial locations. These values were shown as horizontal blue lines along with the direct measurement results in Fig. 9. The direct measurement results of Fig. 9 results show less location dependence than what the wave-theory results of Fig. 11 predicts, but overall, the quantitative agreement between the wave-theory analysis and the direct measurement results for Z_{mass} is reasonable.

Finally, we use the wave analysis to find the effective stiffness of the crista acustica tissue. As noted above, in a wave system, KE and PE are equal. $KE = (1/2)\rho h_{\text{eff}}\omega^2 x^2$ and $PE = (1/2)S_{\text{eff}}x^2$, where S_{eff} is a “specific acoustic stiffness” with units of Pa/m. Equating KE and PE gives $S_{\text{eff}} = \rho h_{\text{eff}}\omega^2$. S_{eff} is shown in Fig. 12. The stiffness is greater in distal than in proximal regions. Stiffness is frequency dependent. We discuss these characteristics of the stiffness and compare it to the mammalian cochlea in the Discussion below.

DISCUSSION

The measurements of fluid pressure and tissue motion reported here were undertaken with an aim to measure the physical properties governing traveling-wave propagation in the bushcricket crista acustica. That goal was complicated by our inability to measure the pressure within the acoustic trachea, which was needed to find the pressure difference across the sensory tissue. With pressure difference and tissue velocity measurements, we could have directly calculated the transverse stiffness of the crista. A different strategy for measuring crista acustica stiffness was then followed, based on wave-theory analysis (23,24,34,38) and using previous measurements in which the waveforms of crista acustica motion had been observed at many frequencies. The experimental results of pressure and motion were still useful in that they produced a measure of Z_{mass} , and this quantity was also predicted by the wave theory. The reasonable agreement lent confidence to the wave-theory analysis, which was then applied to produce new findings on the nature of crista acustica stiffness. From Fig. 12, the stiffness is greater in the distal region than in the proximal region. This

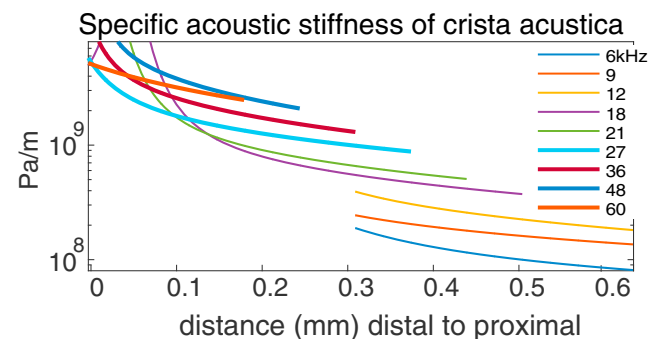


FIGURE 12 Specific acoustic stiffness of the crista acustica found with the wave analysis. To see this figure in color, go online.

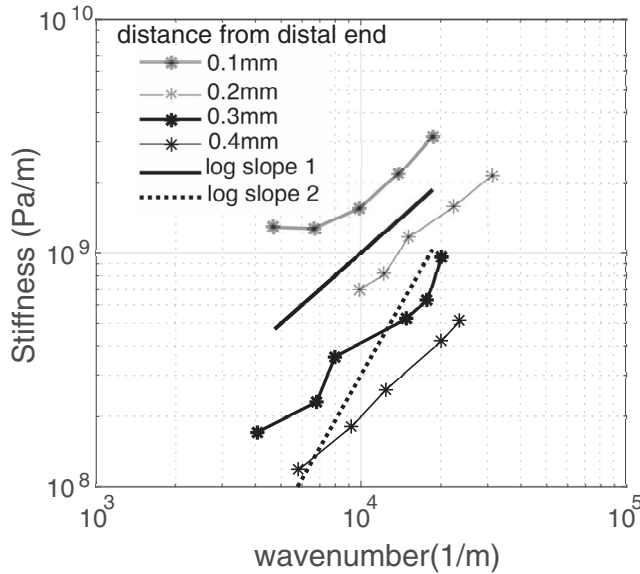


FIGURE 13 Specific acoustic stiffness versus wavenumber at locations 0.1, 0.2, 0.3, and 0.4 mm from the distal end of the crista acustica. Also plotted are lines for stiffness $\sim k$ and stiffness $\sim k^2$.

is expected, based on the longitudinal variation of the anatomical parameters in *M. elongata* (4,9) and on the fact that in the motion responses, high frequencies peak in the distal region, and low frequencies peak in the proximal region. Second, the stiffness values, 10^8 – 5×10^9 Pa/m, are in the same range as in the mammalian cochlea, where the stiffness of the organ of Corti complex in the base was $\sim 5 \times 10^9$ Pa/m (39) and ~ 2 orders of magnitude smaller at a longitudinal location approximately halfway to the apex (40). Another finding is that at a given location, the stiffness increases with increasing frequency. This is different than in the mammalian cochlea and bears further analysis, which follows.

In Fig. 13, we show the stiffness at several longitudinal locations, plotted versus wavenumber. In a string wave, with longitudinal tension governing transverse stiffness, S_{eff} goes as k^2 , and we include a dashed line to indicate that dependence. In a cochlea without longitudinal coupling, S_{eff} is independent of k . The bushcricket crista stiffness is in between those two, with S_{eff} varying approximately linearly with k . The finding that S_{eff} increases with increasing k (and increasing frequency) indicates that there is substantial longitudinal coupling in the bushcricket crista acustica. In the mammalian cochlea, the pronounced transverse anatomy of the basilar membrane's fibers creates a structure with relatively little longitudinal coupling, and the absence of pronounced longitudinal coupling—in other words, the absence of k dependence in the stiffness—is what allows for the sharp apical cutoff of the wave beyond the best place of a given frequency (34,41). The bushcricket crista acustica does not contain a basilar membrane with prominent transverse structure, and it is to be expected that longitudinal

coupling would be relatively large, giving rise to a k -dependent stiffness. In fact, the longitudinal tilt of the scolopodial unit, coupled to the phase gradient produced by the traveling wave, is thought to be important for neural excitation in the bushcricket ear (12). In mammals, a degree of longitudinal coupling conferred by the longitudinal tilt of the Deiters and outer hair cells has been used in cochlear models to activate cochlear amplification (35). Overall, the mammalian and bushcricket ears have key similarities as well as key differences.

Another quantity revealed by the wave analysis is wave speed. In Fig. 14 A, the k data from Fig. 10 are plotted versus frequency at four locations: 0.1, 0.2, 0.3, and 0.4 mm from the distal end. At 0.1 and 0.2 mm, the included frequencies span from 18 to 50 kHz; at 0.3 mm, they span from 6 to 37 kHz; and at 0.4 mm, they span from 6 to 21 kHz. In Fig. 14 B, the k versus frequency data are replotted as radian frequency ($\omega = 2\pi f$, where f is in Hz) versus k . From this plot, the wave's group velocity $d\omega/dk$ was found. At each location, the slope was almost constant, indicating the group velocity, which is the same thing as wave speed when the $d\omega/dk$ slope is constant, did not vary significantly with frequency. The wave speed decreased from the distal to the proximal locations, and at the distances 0.1, 0.2, 0.3, and 0.4 mm from the distal end, we found the following values for wave speed: 13.5, 8.7, 7.5, and 5.2 m/s. Wave speed is expected to be higher in regions of greater stiffness (23), and the stiffness and wave speed trends are as expected, based on the anatomy of the bushcricket crista acustica (4,9). The nearly constant wave speed with frequency at each location is very different from the mammalian cochlea, where the wave speed is much slower at the frequency close to a given location's best frequency than at lower frequencies. For example, in the chinchilla base, the traveling wave speed was ~ 100 m/s for frequencies well below the best frequency and ~ 8 m/s close to the best frequency (42). The nearly frequency-independent wave speed in the bushcricket ear emerges from the finding that the stiffness is proportional to k . Going back to the section equating KE and PE , we had $KE = (1/2)\rho h_{eff}\omega^2 x^2$ and $PE = (1/2)S_{eff}x^2$. We noted that the 2D expression for h_{eff} was similar to the complex 3D result, and we use the 2D expression here to keep this explanation appropriately short and transparent and write $h_{eff} = 1/k$. For bushcricket, $S_{eff} = S_o k$. Equating PE and KE gives $(1/2)(\rho/k)\omega^2 x^2 = (1/2)S_o k x^2$, which simplifies to $\omega/k = \sqrt{S_o/\rho}$, a nondispersive wave, whose wave speed is the same for all frequencies. Contrast that with the mammalian cochlea, treated with the same simplification, $h_{eff} = 1/k$. In the mammalian cochlea, to first order, S_{eff} does not depend on k , so we write $S_{eff} = S_o$. Then, equating KE and PE , we arrive at $d\omega/dk = (1/2\omega)S_o/\rho$, a dispersive wave whose wave speed decreases with frequency (38).

In both the bushcricket and the mammalian cochlea, as the traveling wave moves from regions of higher to regions

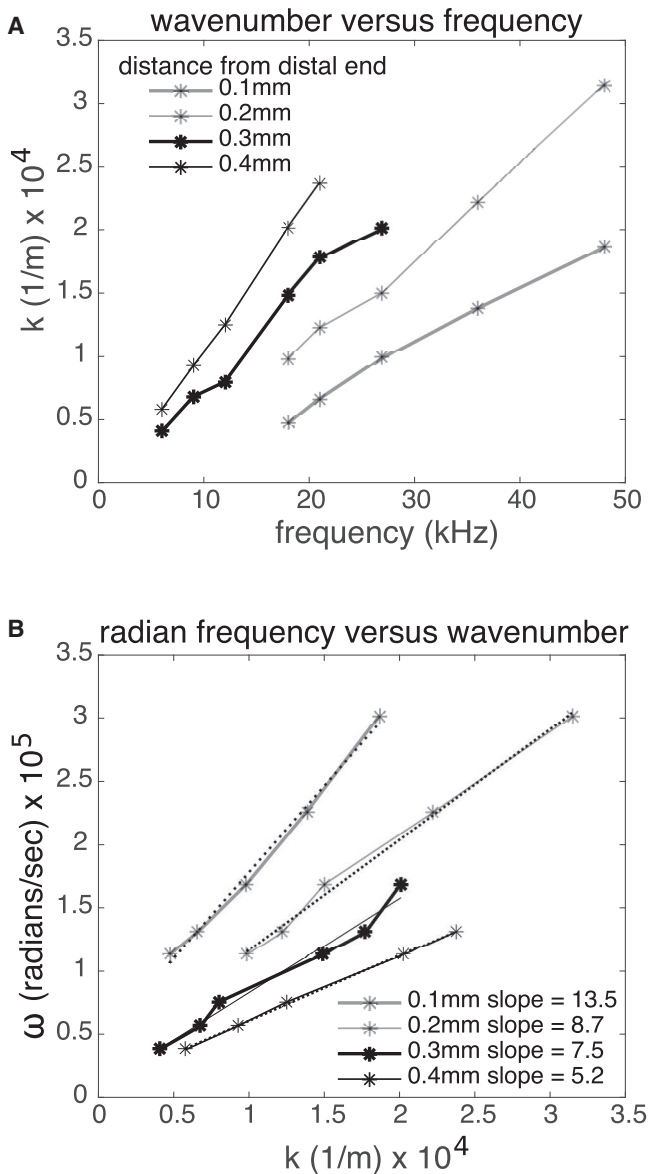


FIGURE 14 Local wavenumber of the traveling wave at different position along the crista acustica. (A) The k data from Fig. 10 are plotted versus frequency at four locations, 0.1, 0.2, 0.3, and 0.4 mm from the distal end. (B) The k versus frequency data are replotted as radian frequency ($\omega = 2\pi f$, where f is in Hz) versus k . From this plot, the wave's group velocity, the slope of ω versus k , was found.

of lower stiffness, it slows, and its motion amplitude grows. In both systems, at some point, the amplitude peaks and drops off, and that point is reached sooner for higher frequency. In both systems, beyond the drop-off, a uniphasic motion mode emerges. In both systems, the precise reason for the drop-off is not well understood. In mammals, the drop-off is usually attributed to the increasing impact of damping, and damping is a candidate in the bushcricket as well. Close to the tissue, fluid viscosity will produce substantial damping, especially when tissue layers move with respect to each other (43,44).

It is notable that the indirect method for measuring the stiffness of the bushcricket hearing organ we employed, using a measurement of effective mass and then applying the energy balance concepts of traveling waves, resulted in a different result than if we had managed to do the measurement we had originally planned to do. We had hoped to measure stiffness by measuring the transverse pressure difference across the cristae and dividing that quantity by the displacement of the cristae. However, that measurement would most likely not have discerned the k -dependent stiffness that the wave analysis found. The observed k -dependent stiffness indicates that the relevant stiffness for the traveling wave of the bushcricket ear is due to longitudinal tension in the organ, and thus this tension is a significant force in addition to the transverse pressure difference. Ultimately, however, the pressure in the acoustic trachea is the drive to the ear, and the originally planned measurement would still be very interesting to more fully understand how acoustic energy is processed by the bushcricket ear.

We end by turning our attention back to the subject of this study, the bushcricket. It is remarkable that the bushcricket crista acustica is able to sort frequencies ranging from 3 to 80 kHz over a length that is shy of 1 mm. Compare this to the mouse, for which a similar frequency range is represented over a basilar membrane ~ 1 cm in length (45,46). The bushcricket collects this tuned information by just 45 sensory neurons compared to the mouse ear with $\sim 15,000$ auditory neurons. Although the ability to sort frequency over a wide frequency range is available to the bushcricket, fine frequency resolution at the neural level is not. Bushcrickets are able to discriminate intra-(21) and interspecific (47) sound signals for mate finding or predator avoidance, respectively. This simple differentiation between potentially attractive or aversive sound sources is made by the activation of a small number of neurons in the prothoracic ganglion and brain, induced by the spiking activity of the auditory neurons (48). Complex sound processing that the mouse uses for social interaction and the integration of the sound-induced signal by multiple brain regions is not present in the bushcricket or necessary for the straightforward auditory tasks it performs.

The theory of the cochlear traveling wave is one of the beautiful outcomes of the fundamental observations of von Békésy (14), and the complete wave patterns that were available from the bushcricket provided a rich source of experimental data with which to apply the theory of fluid-mechanical traveling waves. The basic similarities between bushcricket and mammalian hearing organs reaffirm that a fundamental characteristic of many sound sensing systems, composed of flexible tissue submerged in fluid, is that they support waves, which can be used to transport the sound stimulus along the tissue and sort it mechanically by frequency.

AUTHOR CONTRIBUTIONS

Both authors contributed to the design of the experiments, data acquisition and analysis, and preparation of the manuscript.

ACKNOWLEDGMENTS

The authors thank Michael Carapezza and Sushrut Kale for helpful support during sensor preparation and measurements.

M.N. was funded by a Deutsche Forschungsgemeinschaft grant NO 841/11-1. E.S.O. was funded by the National Institutes of Health grant R01 DC015362 and the Emil Capita foundation.

REFERENCES

- Rössler, W. 1992. Functional morphology and development of tibial organs in the legs I, II and III of the bushcricket *Ephippiger ephippiger* (Insecta, Ensifera). *Zoomorph.* 112:181–188.
- Rössler, W. 1992. Postembryonic development of the complex tibial organ in the foreleg of the bushcricket *Ephippiger ephippiger* (Orthoptera, Tettigoniidae). *Cell Tissue Res.* 269:505–514.
- Kalrmring, K., W. Rössler, ..., R. Lakes. 1992. Structure, receptor cell arrangement and function of the auditory organs in the foreleg tibia of three bushcricket species. *Acta Biol. Hung.* 43:441–449.
- Kalrmring, K., W. Rössler, ..., R. Lakes. 1993. The auditory receptor organs in the forelegs of bushcrickets: physiology, receptor cell arrangement, and morphology of the tympanal and intermediate organs in three closely related species. *Zool. Jb. Physiol.* 97:75–94.
- Lin, Y., K. Kalrmring, ..., W. Rössler. 1993. Auditory receptor organs in the forelegs of *Gampsocleis gratiosa* (Tettigoniidae): morphology and function of the organs in comparison to the frequency parameters of the conspecific song. *J. Exp. Zool.* 267:377–388.
- Rössler, W., A. Hübschen, ..., K. Kalrmring. 1994. Functional morphology of bushcricket ears: comparison between two species belonging to the Phaneropterinae and Decticinae (Insecta, Ensifera). *Zoomorph.* 114:39–46.
- Sickmann, T., K. Kalrmring, and A. Müller. 1997. The auditory-vibratory system of the bushcricket *Polysarcus denticauda* (Phaneropterinae, Tettigoniidae). I. Morphology of the complex tibial organs. *Hear. Res.* 104:155–166.
- Strauß, J., G. U. Lehmann, ..., R. Lakes-Harlan. 2012. Spatial organization of tettigoniid auditory receptors: insights from neuronal tracing. *J. Morphol.* 273:1280–1290.
- Hummel, J., M. Kössl, and M. Nowotny. 2017. Morphological basis for a tonotopic design of an insect ear. *J. Comp. Neurol.* 525:2443–2455.
- Palghat Udayashankar, A., M. Kössl, and M. Nowotny. 2012. Tonotopically arranged traveling waves in the miniature hearing organ of bushcrickets. *PLoS One.* 7:e31008.
- Palghat Udayashankar, A., M. Kössl, and M. Nowotny. 2014. Lateralization of travelling wave response in the hearing organ of bushcrickets. *PLoS One.* 9:e86090.
- Hummel, J., S. Schöneich, ..., M. Nowotny. 2016. Gating of acoustic transducer channels is shaped by biomechanical filter processes. *J. Neurosci.* 36:2377–2382.
- Sarria-S, F. A., B. D. Chivers, ..., F. Montealegre-Z. 2017. Non-invasive biophysical measurement of travelling waves in the insect inner ear. *R. Soc. Open Sci.* 4:170171.
- von Békésy, G. 1960. *Experiments in Hearing*. McGraw Hill, New York.
- Zhantiev, R. D. 1971. Frequency characteristics of tympanal organs in grasshoppers (Orthoptera, Tettigoniidae). *Zool. Zh.* 50:507–514.
- Oldfield, B. P. 1982. Tonotopic organisation of auditory receptors in Tettigoniidae (Orthoptera: Ensifera). *J. Comp. Physiol.* 147:461–469.
- Oldfield, B. P. 1984. Physiology of auditory receptors in two species of Tettigoniidae (Orthoptera: Ensifera). *J. Comp. Physiol. A.* 155:689–696.
- Römer, H. 1987. Representation of auditory distance within a central neuropil of the bushcricket *Mygalopsis marki*. *J. Comp. Physiol. A.* 161:33–42.
- Stumpner, A. 1996. Tonotopic organization of the hearing organ in a bushcricket. *Naturwiss.* 83:81–84.
- Stölting, H., and A. Stumpner. 1998. Tonotopic organization of auditory receptors of the bushcricket pholidoptera griseoptera (Tettigoniidae, decticinae). *Cell Tissue Res.* 294:377–386.
- Scherberich, J., J. Hummel, ..., M. Nowotny. 2017. Functional basis of the sexual dimorphism in the auditory fovea of the duetting bushcricket *Ancylecha fenestrata*. *Proc. Biol. Sci.* 284:20171426.
- Olson, E. S. 2013. Fast waves, slow waves and cochlear excitation. *Proc. Meet. Acoust.* 19:05134.
- deBoer, E. 1984. Auditory physics. Physical principles in hearing theory. II. *Phys. Rep.* 105:141–226.
- Steele, C. R., and L. A. Taber. 1979. Comparison of WKB calculations and experimental results for three-dimensional cochlear models. *J. Acoust. Soc. Am.* 65:1007–1018.
- Dallos, P. 1992. The active cochlea. *J. Neurosci.* 12:4575–4585.
- Patuzzi, R. 1996. Cochlear micromechanics and macromechanics. In *The Cochlea*. P. Dallos, A. N. Popper, and R. R. Fay, eds. Springer-Verlag, pp. 186–257.
- Vater, M., and M. Kössl. 2011. Comparative aspects of cochlear functional organization in mammals. *Hear. Res.* 273:89–99.
- Lim, D. J. 1980. Cochlear anatomy related to cochlear micromechanics. A review. *J. Acoust. Soc. Am.* 67:1686–1695.
- Schumacher, R. 1975. Scanning-electron-microscope description of the tibial tympanal organ of the Tettigoniidae (Orthoptera, Ensifera). *Z. Morphol. Tiere.* 81:209–219.
- Vincent, J. F., and U. G. Wegst. 2004. Design and mechanical properties of insect cuticle. *Arthropod Struct. Dev.* 33:187–199.
- Olson, E. S. 1998. Observing middle and inner ear mechanics with novel intracochlear pressure sensors. *J. Acoust. Soc. Am.* 103:3445–3463.
- Olson, E. S., and H. H. Nakajima. 2015. A family of fiber-optic based pressure sensors for intracochlear measurements. *Proc. SPIE.* 9303:1–7.
- Olson, E. S. 1999. Direct measurement of intra-cochlear pressure waves. *Nature.* 402:526–529.
- Lighthill, J. 1981. Energy flow in the cochlea. *J. Fluid Mech.* 106:149–213.
- Yoon, Y. J., C. R. Steele, and S. Puria. 2011. Feed-forward and feed-backward amplification model from cochlear cytoarchitecture: an interspecies comparison. *Biophys. J.* 100:1–10.
- de La Rochefoucauld, O., and E. S. Olson. 2007. The role of organ of Corti mass in passive cochlear tuning. *Biophys. J.* 93:3434–3450.
- de Boer, E., and E. van Bienenma. 1982. Solving cochlear mechanics problems with higher-order differential equations. *J. Acoust. Soc. Am.* 72:1427–1434.
- Siebert, W. M. 1974. Ranke revisited—a simple short-wave cochlear model. *J. Acoust. Soc. Am.* 56:594–600.
- Dong, W., and E. S. Olson. 2009. In vivo impedance of the gerbil cochlear partition at auditory frequencies. *Biophys. J.* 97:1233–1243.
- Naidu, R. C., and D. C. Mountain. 1998. Measurements of the stiffness map challenge a basic tenet of cochlear theories. *Hear. Res.* 124:124–131.
- Taber, L. A., and C. R. Steele. 1981. Cochlear model including three-dimensional fluid and four modes of partition flexibility. *J. Acoust. Soc. Am.* 70:426–436.
- Rhode, W. S., and A. Recio. 2000. Study of mechanical motions in the basal region of the chinchilla cochlea. *J. Acoust. Soc. Am.* 107:3317–3332.

43. Prodanovic, S., S. Gracewski, and J. H. Nam. 2015. Power dissipation in the subreticular space of the mammalian cochlea is modulated by inner hair cell stereocilia. *Biophys. J.* 108:479–488.
44. Wang, Y., and E. S. Olson. 2016. Cochlear perfusion with a viscous fluid. *Hear. Res.* 337:1–11.
45. Koay, G., R. Heffner, and H. Heffner. 2002. Behavioral audiograms of homozygous med(J) mutant mice with sodium channel deficiency and unaffected controls. *Hear. Res.* 171:111–118.
46. Burda, H., L. Ballast, and V. Bruns. 1988. Cochlea in old world mice and rats (Muridae). *J. Morphol.* 198:269–285.
47. Schul, J., F. Matt, and O. von Helversen. 2000. Listening for bats: the hearing range of the bushcricket *Phaneroptera falcata* for bat echolocation calls measured in the field. *Proc. Biol. Sci.* 267:1711–1715.
48. Stumpner, A., and M. Nowotny. 2014. Neural processing in the bushcricket auditory pathway. *In Insect Hearing and Acoustic Communication*. B. Hedwig, ed. Springer, pp. 143–166.